Use of Radar Chaff for Studying Circulations in and around Shallow Cumulus Clouds

EUNSIL JUNG AND BRUCE ALBRECHT

Rosenstiel School of Marine and Atmospheric Science, University of Miami, Miami, Florida

(Manuscript received 24 July 2013, in final form 20 April 2014)

ABSTRACT

Circulations in and around cumulus clouds are inferred by using a passive tracer (radar chaff) and an airborne cloud radar during the Barbados Aerosol Cloud Experiment (BACEX). The radar chaff elements used for this experiment are fibers that are cut to a length of about ½ of the radar wavelength to maximize radar returns by serving as dipole antennas. The fibers are packed in fiber tubes and are mounted in a dispenser beneath the wing of the aircraft. The chaff was released near the tops and edges of a growing small cumulus cloud. The aircraft then made penetrations of the cloud at lower levels to observe the chaff signals above the aircraft with the zenith-pointing cloud radar. This study shows that the environmental air above the cloud top descends along the downshear side of the cloud edge and is subsequently entrained back into the same cloud near the observation level. The in-cloud flow follows an inverted letter P pattern. The merits and limitations of the chaff method for tracking circulations in and around small cumuli are discussed.

1. Introduction

Entrainment influences cloud characteristics and processes, and can impact cloud lifetime, cloud radiative properties, electrification of clouds, cloud chemistry, etc. Entrainment and the resulting mixing processes (e.g., Baker et al. 1980; Carpenter et al. 1998; Gerber et al. 2008; Lehmann et al. 2009; Wang et al. 2009; Lu et al. 2011) are important in affecting cloud microphysics and dynamics. For example, these processes can influence the evolution of the cloud droplet size distribution and the formation of precipitation (e.g., Lasher-Trapp et al. 2005; Cooper et al. 2013). These effects have been studied through observations [e.g., source level of entrained air by Paluch (1979), Blyth et al. (1988), Jonas (1990), Blyth (1993), Damiani et al. (2006), and Lehmann et al. (2009)], laboratory experiments [e.g., mixing characteristics of turbulent thermals by Johari (1992)], and numerical simulations [e.g., a study of the life cycles of shallow cumuli using passive subcloud tracers by Zhao and Austin (2005), the origin of in-cloud air by Heus et al. (2008), and stochastic entrainment behavior by Romps and Kuang (2010)]. However, there are continuing debates on the origin of the air entrained into cumulus clouds [e.g., cloud-top mixing vs lateral mixing; see, e.g., Heus et al. (2008)]. Furthermore, the mechanics of how the environmental air is entrained into the cloud and the details of the mixing process are poorly observed. Blyth et al. (1988) suggested that entrainment occurs near the ascending cloud top as clouds grow, and the mixed parcels subsequently descend around the edge of the advancing thermal core into a trailing wake region driven by a toroidal circulation. Conversely, Jonas (1990) showed that the environmental air from near cloud top is transported to a lower level and then laterally entrained into the cloud.

Using two conserved parameters that mix linearly, Paluch diagrams (Paluch 1979) are often used to identify the source level of air entrained into the cloud. However, there are problems and/or restrictions in using Paluch diagrams. First, the saturation assumption of the cloudy air in the shallow marine cumulus cloud may not be satisfied (Jensen and Blyth 1988) and can lead to misinterpretation. Second, the exposure of the temperature sensor to cloud water can introduce an artificial cooling into the cloud and upon exit into an unsaturated environment. As a result, the wetting of the temperature sensor (e.g., Wang and Geerts 2009) can affect the interpretation of the diagram and estimates of buoyancy in the cloud by overestimating the entrainment and underestimating the buoyancy. Third, the environmental air should be well represented by the soundings that

Corresponding author address: Eunsil Jung, RSMAS/MPO, University of Miami, 4600 Rickenbacker Cswy., Miami, FL 33149.
E-mail: eunsil.jung@gmail.com

DOI: 10.1175/JAMC-D-13-0255.1

are used in the Paluch diagrams, since the air in the sounding represents the environmental air that entrains into the cloud; however, a true measure of the representative environmental air is often difficult to obtain. Finally, commonly used slow-response humidity sensors can limit the use of the humidity measurements needed for the Paluch diagrams.

However, there are more direct methods using physical tracers in the atmosphere. For example, Stith (1992) used sulfur hexafluoride (SF_6) as a tracer to study the entrainment mechanism. The gas was released from an aircraft that flew above growing convective turrets, and was sampled by a second aircraft flying at a level far below the cloud top. For each of the clouds studied, the maximum concentration of SF_6 was first found along the outside of the cloud edges and, then, in the central portions of the turrets. Moninger and Kropfli (1987) suggested a measurement technique using a dual-polarization scanning radar and microwave-reflecting chaff. Although they did not demonstrate the actual circulations in and around the clouds, they showed how radar returns from chaff that was released near a thunderstorm could be used to distinguish hydrometer returns from chaff. Further, they provided a list of scientific questions that could be addressed by using chaff as a tracer, but there have been no subsequent studies made to demonstrate the merit of the radar chaff technique to address these questions.

Therefore, the focus of this study is on the application of radar chaff as a tracer for studying circulations in and around small cumulus clouds. We use the radar chaff as a passive tracer to demonstrate how the entrainment process can be examined. Questions that are investigated with this technique, which are demonstrated here for a single cloud, include the following: 1) Where does entrainment primarily occur in cumulus clouds (lateral vs cloud-top entrainment)? 2) Are there specific entrainment levels? 3) Once in the cloud, where does entrained air go? The data used in this study were obtained during the Barbados Aerosol Cloud Experiment 2010 (BACEX) from the Center for Interdisciplinary Remotely Piloted Aircraft Studies (CIRPAS) Twin Otter research aircraft that was equipped with an upward-facing (zenith viewing) cloud radar and standard meteorological instruments (e.g., Jung et al. 2013). Chaff was dispensed for several individual clouds and in the clear-air boundary layer during BACEX. In this study, a shallow marine cumulus cloud (cloud depth $<$ 1 km) observed about 50–100 km east of Barbados on 29 March 2010 was documented in detail to demonstrate the feasibility of using radar chaff as a means to study entrainment processes and small-scale circulations in and around small cumuli.

2. Data and methods

a. Aircraft data

The Barbados Aerosol Cloud Experiment was performed from 15 March to 15 April 2010 in the trades of the Atlantic. The principal observing platform for the experiment is the CIRPAS Twin Otter research aircraft that was equipped with 1) probes that measure aerosol, clouds, and precipitation (Fig. 1a); 2) standard meteorological instruments that observe the atmospheric thermodynamic and wind structures; and 3) a zenith-pointing, bistatic 95-GHz frequency-modulated continuous-wave Doppler radar (i.e., cloud radar) that yields fine vertical structures of updrafts and downdrafts in clouds. The cloud radar was designed and fabricated by ProSensing, Inc., and is mounted on top of the aircraft, perpendicular to the centerline (Fig. 1b). The aerosol, cloud, and precipitation probe data are obtained at 1-Hz resolution, and the meteorological variables (temperature, humidity, winds, Gerber probe liquid water content, etc.) were acquired at both 1- and 10-Hz resolutions. The radar data were obtained with a sampling rate of 3 Hz (temporal resolution) with range gates at 24 m (spatial resolution), an antenna beamwidth of 0.7°, and a velocity resolution of 0.16 m s^{-1}. The radar has a dead zone of about 50 m, which allows radar observations to be made in close proximity to the in situ probe measurements. The radar's minimum detectable sensitivity is -27 dBZ at 1 km. The airborne cloud radar used in this study is an important tool that provides precipitation properties and vertical structures of updrafts and downdrafts within the clouds. To make full use of this tool, velocity corrections due to the aircraft motions and reflectivity calibrations were made. For details on the motion corrections and reflectivity calibrations, see Jung (2012).

The temperature and dewpoint temperature data were obtained from the Rosemount temperature sensor and an EdgeTech chilled mirror device, respectively (http://www.cirpas.org/instrumentList.html). There is evidence that the temperature sensors used on the aircraft (e.g., the Rosemount temperature sensor in this study, and the reverse-flow immersion thermometers in the Rain in Cumulus over the Ocean field campaign) become wet in cumulus clouds (e.g., Eastin et al. 2002; Wang and Geerts 2009), leading to erroneously low temperatures during the exit from a cloud as well as in the cloud because of evaporative cooling. Further, a fast-response humidity sensor was not available during the experiment, and thus, a time lag in the moisture data was observed (not shown). Consequently, we do not include a Paluch diagram analysis in this study. A summary of the instruments used on the Twin Otter for the experiment is given in Table 1.

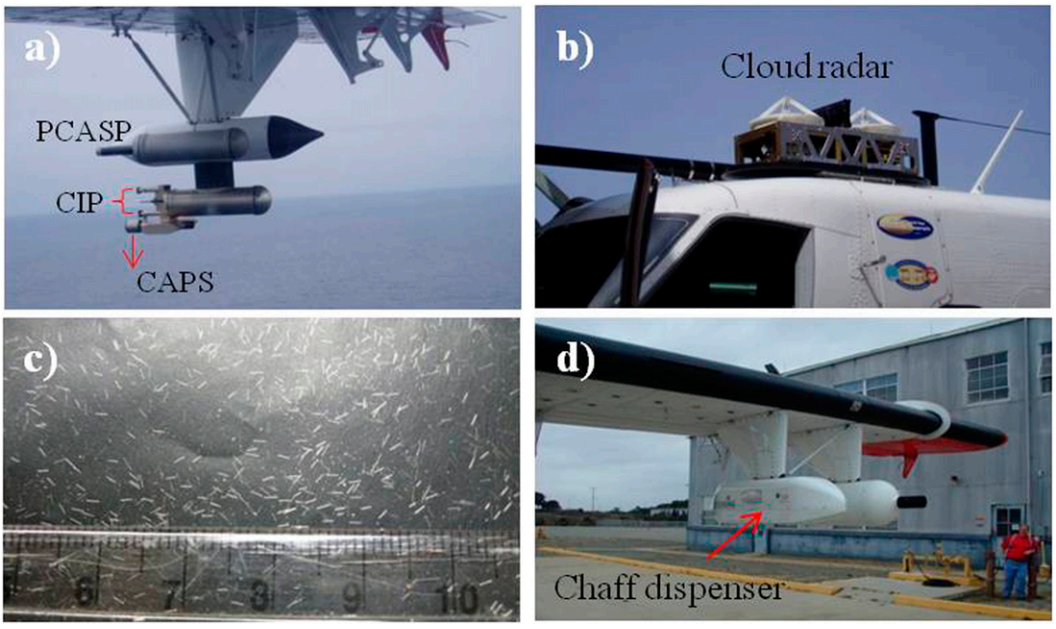

FIG. 1. (a) Cloud, aerosol, and precipitation probe sensors attached to the underside of the right wing of the CIRPAS Twin Otter research aircraft. (b) The cloud radar mounted on top of the airplane. (c) Chaff fibers used in this study for 95-GHz radar (labels on ruler are in centimeters). (d) Chaff dispenser attached beneath the left wing of the CIRPAS research aircraft.

b. Passive tracer method

To study the entrainment process and the origin of the entrained air, a passive tracer (radar chaff) is used. The radar chaff elements used for this experiment are metal-coated Mylar fibers that are cut to a length of about ½ of the radar wavelength (about 1.5 mm; see Fig. 1c) to maximize radar returns by serving as dipole antennas (Zrnić and Ryzhkov 2004).

The chaff fibers are packed in fiber tubes (14-cm length × 3.5-cm diameter), and are mounted in a dispenser (ALE-47 Airborne Countermeasures Dispenser System) that holds a maximum of 24 tubes beneath the left wing of the aircraft (Fig. 1d). Chaff from each of the tubes is dispersed into the airstream by a small explosive charge that is detonated on command. Visually, the chaff release appears as a line of chaff emanating from the chaff dispenser. In this study, chaff was released near the cloud tops and edges of a small cumulus cloud. Since the terminal velocity of the fiber is about 2 cm s^{-1}, it effectively follows air motions. After the chaff fibers were released, the aircraft made penetrations of the cloud at lower levels, to observe the chaff signals above with the upward-facing cloud radar. The sequential penetrations were made using GPS markers to locate the cloud. Although we cannot quantitatively estimate how the chaff line will be dispersed after release, a number of chaff releases were made in clear areas and then sampled by the radar while flying under these areas. Flights crossing beneath the chaff lines about 3.5 min after the releases indicated a chaff plume width of about 200 m with background winds of 8–9 m s^{-1} (see Fig. 3c). The technique is similar to that in Stith (1992), using SF_6, except it can only be detected

TABLE 1. Characteristics of the instruments used in BACEX.

Instrument	Manufacturer	Observations/purpose
Temperature probe	Rosemount	Total temperature
Dewpoint temperature probe	EdgeTech	Dewpoint temperature
Liquid water probe (PVM-100A)	Gerber Scientific, Inc.	Liquid water content of clouds
Cloud radar	Prosensing, Inc.	Doppler spectrum; cloud properties, in-cloud turbulence
Passive Cavity Aerosol Spectrometer Probe (PCASP)	PMS, Inc.	Aerosols, 0.1–2.5 μm, 20 bins
Cloud Aerosol Spectrometer (CAS)	DMT, Inc.	Aerosols and clouds, 0.6–60 μm, 20 bins
Cloud Imaging Probe (CIP)	DMT, Inc.	Drizzle, 25–1550 μm, 62 bins

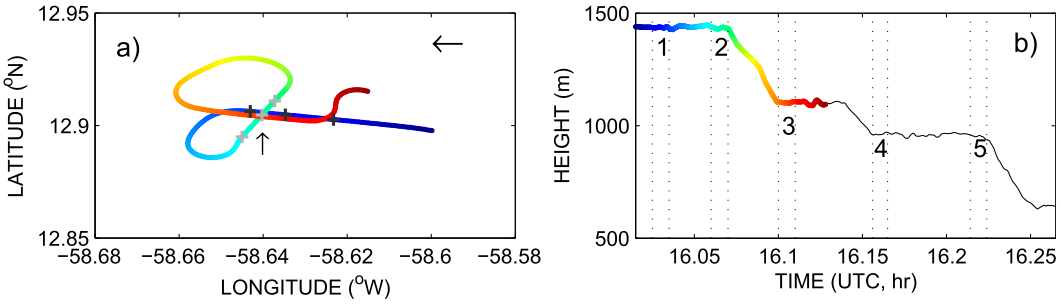

FIG. 2. (a) A flight pattern and (b) corresponding altitude during the chaff experiment. Colors indicate elapsed time (earlier time is denoted as a blue color). The spatial locations where the chaff was released are shown as plus signs in (a) (black, upwind; gray, crosswind), and the target cloud is located at the intersection of the flight paths [ending point of the upward arrow in (a)]. The horizontal arrow (pointing toward left) indicates the direction of the background winds (easterly). The duration of the cloud penetration is denoted with vertical dotted lines in (b). Flight paths after leg 3 are not shown in (a).

where the aircraft transects the gas, whereas in this study the chaff can be detected remotely by a cloud radar anywhere above the zenith-pointing cloud radar. Furthermore, SF_6 can no longer be frequently released, as its usage is banned or limited due to its potency as a greenhouse gas. However, chaff can be released everywhere as long as it is not detected by aircraft navigation radars. The short length of the chaff used here with the cloud radar avoids detection by longer-wavelength radars used for aircraft reconnaissance or weather surveying [for discussion about chaff detection and usage for military applications, see Zrnić and Ryzhkov (2004)].

Flight paths and time series of the altitudes flown on 29 March 2010 for the chaff experiment are shown in Fig. 2. Five sets of cloud penetrations were made and two sets of level legs were made at the same altitude (Fig. 2b, e.g., legs 1 and 2, legs 4 and 5). Here, a level flight leg refers to a cloud penetration flight leg flown at a relatively constant height. Chaff was released at the same levels near the tops of growing cumuli during leg 1 (flying with the wind, shown as black cross symbols in Fig. 2) and leg 2 (flying crosswind, gray cross symbols in Fig. 2). The plane traveled about 60 m horizontally during each chaff release. After the chaff fibers were released, the aircraft made penetrations into the same cloud along legs 3–5; all of which were flown with the wind (Fig. 2b, shown as numerical labels for each level leg). The cloud had nearly disappeared by the fourth penetration (leg 4); thus, only the first four of the five penetrations of the cloud (legs 1–4) are discussed here.

3. Results

a. Mean boundary layer structure

The cloud examined in this study on 29 March 2010 is sampled about 50–100 km east of Ragged Point, the easternmost location in Barbados. A bimodal distribution of cumulus cloud tops with cloud bases around 600 m was observed. In general, the groups of shallower clouds have tops at about 1 km and deeper clouds have tops around 2 km. Many clouds observed on this flight consisted of multiple small thermals with some detrainment occurring near the cloud tops. The accumulation mode aerosol concentrations obtained from the Passive Cavity Aerosol Spectrometer Probe showed aerosol concentrations of less than 200 cm^{-3} near the surface and decreasing with height (not shown). The boundary layer thermodynamic and wind structures are shown in Fig. 3. The vertical profiles were obtained during a descent and an ascent of the aircraft approximately 13–14 and 4 min prior to the initial cloud penetrations, respectively. Profiles were averaged over 2-s intervals to filter out small-scale variability.

The potential temperature θ and mixing ratio r_v from both soundings (Fig. 3) are relatively constant in the subcloud layer (surface to ~600 m). The descent sounding (solid) shows a less variable structure than the later ascent sounding in the cloud layer; θ slightly increases with height and the upper parts of the cloud layers (1400–1750 m) are more unstable than the lower parts of the cloud (LCL–1400 m). The top of the cloud layer is capped by an inversion where the mixing ratio (potential temperature) decreases (increases) rapidly with height at about 1800 m.

The ascent sounding (dashed) shows a more variable vertical structure although no observations were made above 1500 m. An enhanced moisture layer that could be associated with detrainment and/or cloud remnants is observed above 1300 m, which is near the cloud top during the third and fourth cloud penetrations (the third and fourth penetrations correspond to the mature and dissipating stages of the cloud, respectively). The layers below 1300 m (e.g., a layer between ~1050 and 1250 m) possibly inhibit cloud growth and lead to the lower

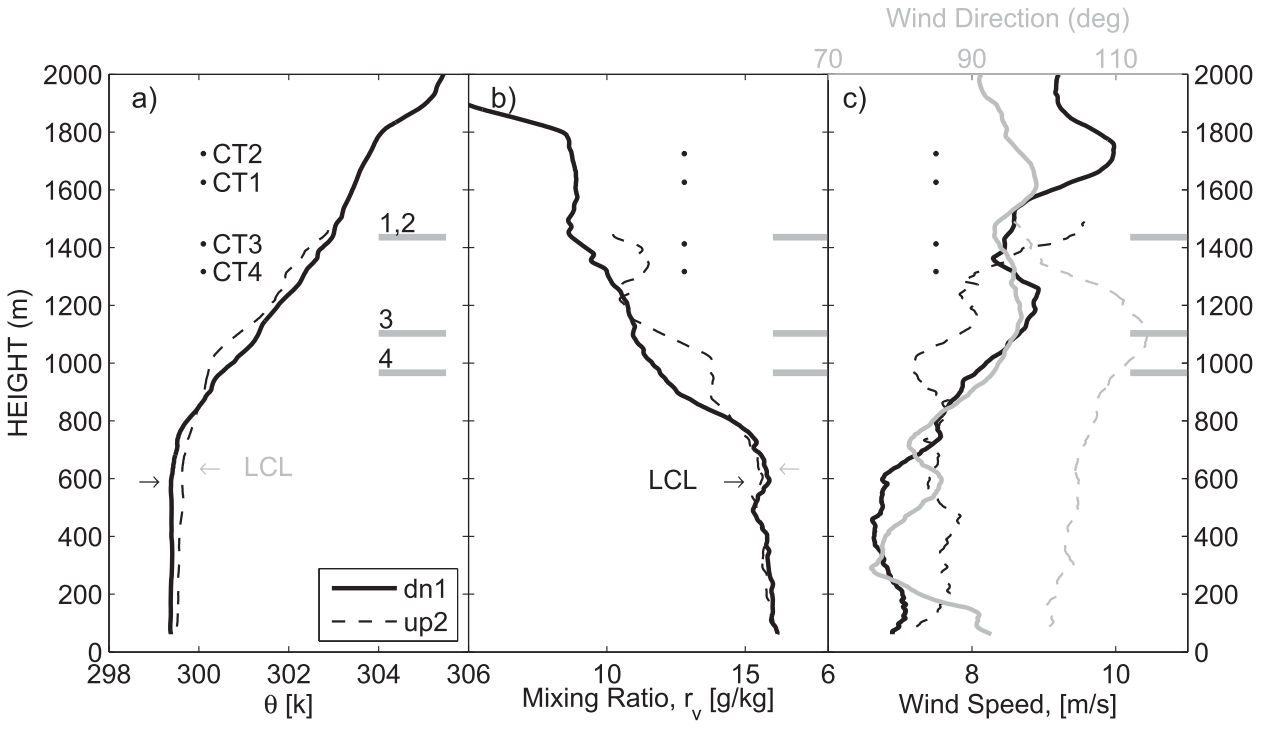

FIG. 3. Profiles of (a) potential temperature θ, (b) water vapor mixing ratio r_v, and (c) winds, obtained from a descent (solid, denoted as dn1; 13.2°N, 58.7°W; 0.3° north of the cloud) and an ascent (dashed, denoted as up2; 12.8°N, 60°W; 0.1° north of the cloud) during 1528–1548 and 1548:54–1558:05 UTC 29 Mar 2010, respectively. The cloud penetration heights are shown as thick gray horizontal lines that are numbered accordingly (e.g., 1 indicates leg 1). LCLs (horizontal arrows) are calculated from the average thermodynamic properties of the 100–200-m layer above the surface. A black- (gray-) colored LCL denotes the LCL of a descent (ascent) sounding. CT1 indicates a cloud-top height estimated from cloud radar while the aircraft makes a level flight for leg 1, and the same notation is used for the other legs [denoted as black dots in (b) and (c)].

cloud-top groups (i.e., cloud population of tops ~1 km). In contrast, once the clouds grow taller than ~1 km, their tops reach ~1800 m, with the aid of possibly enhanced moisture provided from detrainments and/or cloud remnants from the previous clouds [e.g., preconditioning from Bladé and Hartmann (1993)] and less stable atmospheric conditions near cloud tops. The wind on this day was easterly throughout the boundary layer (Fig. 3c), with a vertical shear of ~3 m s^{-1} km^{-1}.

b. *Cloud thermodynamics and dynamics*

The cloud examined for the chaff study was a shallow marine cumulus with a depth of less than 1 km. The multithermal composition of this cloud is clearly evident in the photographs (Fig. 4). These photographs were taken using a camera looking forward out of the cockpit window 10–80 s before the first penetration of the cloud.

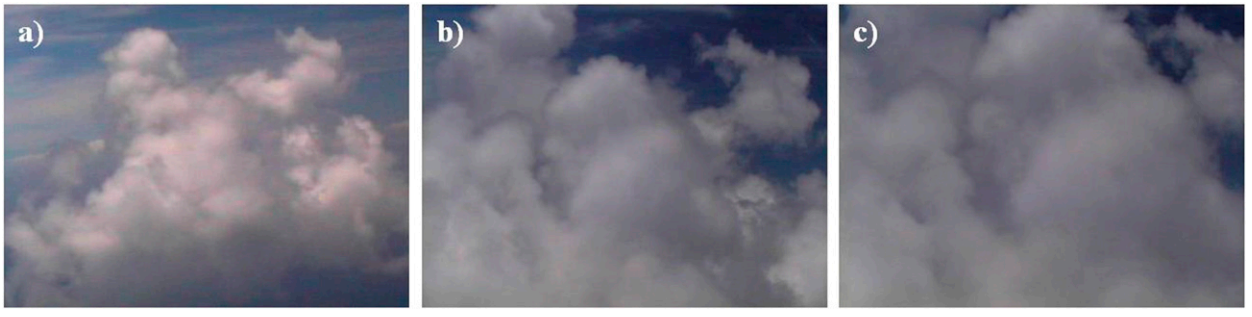

FIG. 4. Photographs taken toward the west, approximately (a) 80, (b) 20, and (c) 10 s prior to the first cloud penetration (leg 1). The airplane penetrated the cloud from east to west during leg 1, and the background wind is into the direction of the photograph (easterly).

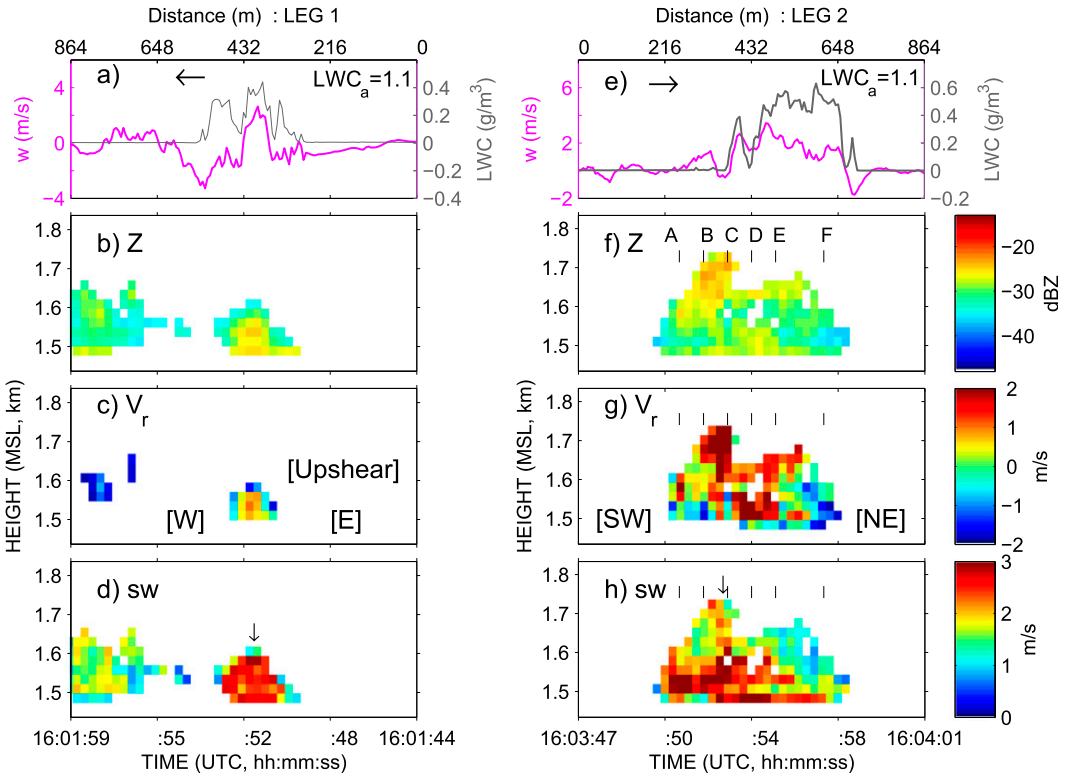

FIG. 5. Time series of (a),(e) LWC (g m^{-3}; gray) and vertical velocity (w, m s^{-1}; magenta) for the cloud penetration during legs (left) 1 and (right) 2. The adiabatic LWC value is shown in the right corner. Time–height cross sections of (b),(f) reflectivity, (c),(g) mean Doppler velocity (positive indicates upward motions), and (d),(h) spectrum width for the chaffed cloud during legs 1 and 2. The cloud penetrations were made at constant heights (along the wind, leg 1; across the wind, leg 2). Horizontal arrows in (a) and (e) indicate the directions of the cloud penetrations. Note that reversed time axes are used during leg 1 to match the penetration direction with the other legs. Vertical dashed lines in (f)–(h) are used to show the locations of Doppler spectra in Fig. 8. We use [E], [W], [NE], and [Upshear] to indicate east, west, and northeast directions and the upshear side. Cloud tops used in this study for legs 1 and 2 are shown with downward-pointing arrows in (d) and (h).

The aircraft made penetrations of the cloud following the wind on legs 1, 3, and 4. Since the radar was mounted on top of the aircraft, the lower penetration heights better capture the full picture of the cloud as well as flows in and around the cloud. During legs 1 and 2, the aircraft made penetrations near the cloud top and was unable to measure the cloud circulations. On leg 3, however, a much larger portion of the cloud was detected as the aircraft penetrated the middle–lower parts of the cloud (Fig. 3). During leg 4, the cloud was near the end of its life and almost dissipated. Taking these points into consideration, the cloud penetration during leg 3 is used as a reference; thus, reversed time axes are used for legs 1 and 4 to match up the cloud features in the spatial direction. In these depictions, east and upshear corresponds to the right side of the cloud during the time series (e.g., in Figs. 5, 6, and 10). Although the aircraft did not penetrate the cloud at exactly the same location during each cloud pass, the directions (along the wind) are the same during legs 1 and 3 (see Fig. 2a). Thus, the shear between the two legs along the flight track is estimated from the average horizontal wind component between legs 1 and 3 after rearranging the cloud direction. The flight information during each level leg is summarized in Table 2.

The cloud structure near the top is obtained from the zenith-pointing cloud radar during the first two cloud penetrations (legs 1 and 2) at a height of about 1440 m. During these penetrations, cloud tops are about 1600–1700 m (shown as arrows in Figs. 5d,h). Liquid water contents [from a Gerber probe (PVM-100A); Gerber et al. (1994)] and vertical velocity, along the transit through the top of this cloud, are shown in Figs. 5a and 5e.

During the first cloud penetration (Fig. 5a), the liquid water content (LWC) of the cloud reached a maximum value of about 0.4 g m^{-3}. The region where the highest LWC is sampled (~1601:50 UTC) is in an updraft of $w \sim 3$ m s^{-1}. Along the downshear edge of the cloud

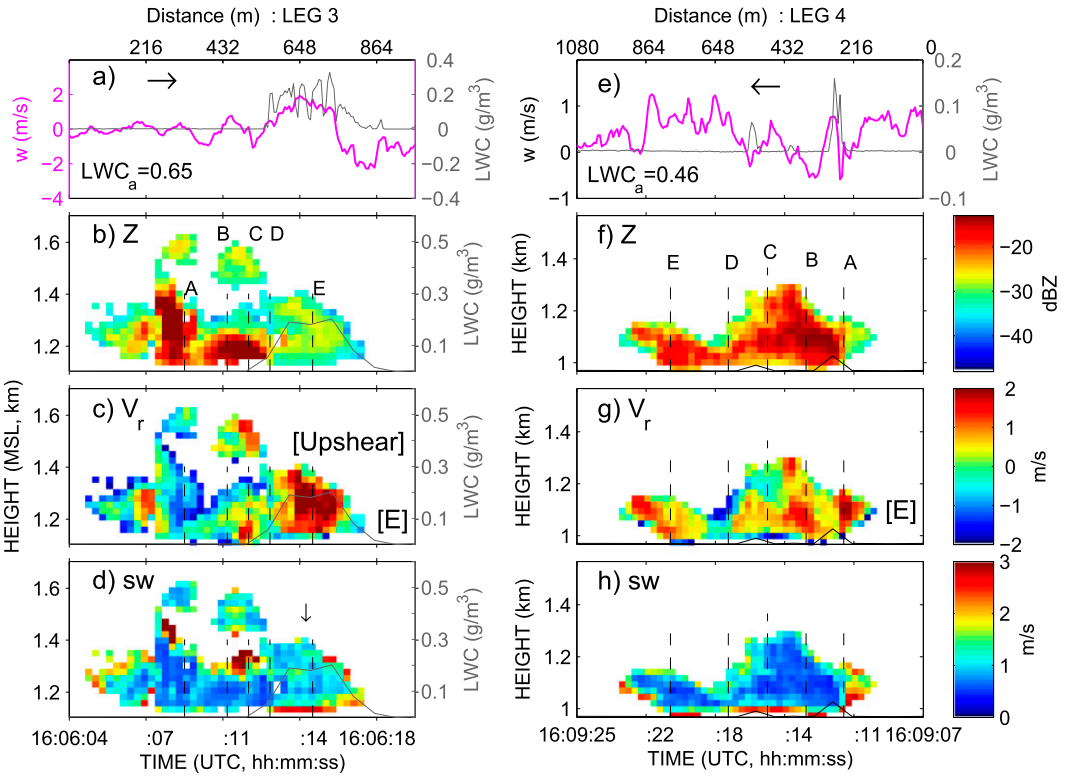

FIG. 6. As in Fig. 5, but for legs (left) 3 and (right) 4. A 1-Hz-resolution Gerber-probe-determined LWC is overlaid on the radar data with the scale shown at the right of the leg-3 plots. Cloud top estimated from leg 3 is shown with a downward-pointing arrow in (d).

(~1601:53 UTC), downdrafts of ~3 m s^{-1} are observed. The velocity calculated from the aircraft's inertial navigation system (e.g., w in Fig. 5a) may not agree with that observed by the cloud radar (e.g., Fig. 5c) mainly because the first usable radar returns are from about 50 m above the aircraft as a result of a dead zone there. In Fig. 5a, the shape of the in-cloud vertical velocity matches the LWC, implying that the cloud elements penetrated at this stage (leg 1; in particular, the middle parts of the cloud elements) are growing (e.g., Lehmann et al. 2009). The adiabatic liquid water content (LWC$_a$) during leg 1 is about 1.1 (±0.05) g m^{-3}, and the ratio of LWC$_{max}$ to LWC$_a$ is 0.36. The leg-1 penetration was made at a height of about 1440 m near an ascending cloud top (1601:49–53 UTC) and radar returns from the cloud were minimal. The radar reflectivity, however, indicates that cloud tops extend to about 1.6 km (MSL). In Figs. 5b,c, relatively stronger reflectivity (~−28 dBZ) with updrafts (Fig. 6b) was observed in the interior of the cloud, surrounded by weaker reflectivity (~−38 dBZ) associated with cloud shell downdrafts. There are some radar echoes at 1601:55–59 UTC; these returns could be from a nearby cloud or cloud remnants since these returns are associated with near-zero vertical velocity (Fig. 5a) or weak downdrafts (Fig. 5c). These echoes are also present in Fig. 6b at 1606:04–07 UTC.

TABLE 2. Summary of flights during the level-leg flights.

Leg No.	Penetration height (m)	Penetration direction	Note	Cloud-top height (m)
1	1436	Along wind (from E to W), downwind	Chaff fibers are released	1626
2	1434	Crosswind (from SW to NE)	Chaff fibers are released	1725
3	1103	Along wind (from W to E), upwind	Chaff signal is detected (~300 m below the initial penetrations)	1413
4	967	Along wind (from E to W), downwind	Chaff signal is detected (~450 m below the initial penetrations); cloud nearly dissipated	~1300

Chaff was released during leg 1 (and leg 2) so that the radar returns during leg 1 are unaffected by chaff, and thus, the observed reflectivity from −38 to −28 dBZ (green and yellowish colors in Fig. 5b) is exclusively due to cloud droplets. For reference, a reflectivity of about −17 dBZ and/or −20 dBZ is often used to define precipitation from the cloud radar (e.g., Frisch et al. 1995). Further, Jung (2012) showed that nonprecipitating clouds sampled during BACEX are characterized by reflectivity weaker than approximately −30 dBZ (−35 dBZ is the most frequently observed), while precipitating clouds are characterized by reflectivity stronger than −20 dBZ (e.g., Fig. 12 of Jung 2012).

The cloud structure during the second penetration (Fig. 5e), made at the same level as leg 1, also shows that the updrafts are associated with higher LWC (maximum of about 0.6 g m^{-3}), indicating that the cloud is in a growing stage, although this value is still less than the estimated adiabatic content 1.1 (±0.05) g m^{-3} at this height ($LWC_{max}/LWC_a = 0.54$). These subadiabatic values are consistent with the results from previous studies of marine cumulus clouds (e.g., Rauber et al. 2007; Gerber et al. 2008), and may be due to several factors: dilution of the cloud, sampling away from the core of maximum vertical velocity, and uncertainties in the estimate of the adiabatic value due to uncertainties about the cloud-base height.

During leg 2 (about 2 min after the first penetration), chaff was released at the same height as during leg 1. The chaff first descended along the cloud edges (as shown later) and was not detected by the zenith-viewing cloud radar during leg 2. Thus, the radar returns obtained from cloud radar during leg 2 are predominately due to the cloud droplets. Cloud tops extend to about 1700 m during leg 2, which is about 120 m higher than the cloud top observed on leg 1. This is consistent with the idea that the cloud is in a growing stage during leg 2. The radar reflectivity in Fig. 5f ranges from −38 to −25 dBZ with updrafts (Fig. 5g; $V_r > 1$–2 m s^{-1}) and broad spectrum widths (Fig. 5h; spectrum width of 2–3 m s^{-1}). Technically, spectrum width is defined as the standard deviation of the velocity distribution within the volume. Shear, turbulence, and hydrometeor size variability (i.e., variations in droplet fall speeds) can contribute to the broadening of the spectrum width (e.g., Kollias et al. 2001). Thus, in a situation where the shear, turbulence, and variations of droplet fall speeds are small, the spectrum width will be small. In a situation where the variability of those components is large, the spectrum width will be large. For a moving aircraft (or a scanning radar beam), an additional spectrum broadening occurs, and it is proportional to the sine of the antenna beamwidth and the speed of the aircraft (Nastrom 1997; Dehghan and Hocking 2011). The characteristics of the observed spectrum width will be used in the following section to show the difference between hydrometeor radar returns and chaff returns.

The third penetration (Fig. 6a, about 2–3 min after the second penetration) is made about 300 m below the initial penetrations (legs 1 and 2). During this cloud pass, LWC reaches a maximum of ~0.3 g m^{-3} [LWCa ~ 0.65 (±0.05) g m^{-3}], and updrafts are associated with this maximum LWC as indicated by both the aircraft (Fig. 6a) and the radar V_r estimates (Fig. 6c). Downdrafts are found along the cloud edges. There is still good agreement between the updrafts and higher LWCs, but the strengths of the updrafts and maximum LWCs are lower than those during leg 2 (e.g., 2 vs 3 m s^{-1}; 0.3 vs 0.6 g m^{-3}). Cloud tops indicated by the radar extend to about 1400 m, and two small turrets, detached from the main cloud, which are possibly the cloud remnants from the clouds probed during leg 1 and 2, are also seen at about 1400–1600 m between 1606:08 and 1606:13 UTC. Reflectivities of ~−28 dBZ (Fig. 6b) along with updrafts of ~2 m s^{-1} (Fig. 6c), and spectrum widths of ~(1–2) m s^{-1} (Fig. 6d), are observed at around 1606:15 UTC in Fig. 6b (near identifier E). On this upshear side of the cloud, reflectivities are dominated by cloud droplets, as indicated by the strength of the reflectivity and the presence of liquid water. However, the regions of reflectivities greater than −20 dBZ (reddish colors in Fig. 6b) are primarily attributed to returns from chaff and will be discussed in the next section.

The cloud observed during the fourth penetration (leg 4; Fig. 6e) shows a maximum LWC of 0.15 g m^{-3} and was associated with a weak updraft (~0.7 m s^{-1}). The observed cloud during leg 4 was substantially weaker than during previous legs and nearly dissipated [LWC_a ~ 0.46 (±0.05) g m^{-3}]. However, strong reflectivities ($Z > -20$ dBZ in Fig. 6f) with relatively small spectrum widths (sw < 1 m s^{-1} in Fig. 6h) were still present due to the chaff. The maximum height of the returns is about 1300 m, and the geometric patterns of the returns are similar to those observed during leg 3.

c. *Chaff returns*

1) DIFFERENCES BETWEEN HYDROMETEOR AND CHAFF RETURNS

Fundamentally, the cloud radar used in this study cannot distinguish signals from chaff and cloud droplets if they coexist, and it is possible that the radar returns for a given time are from both the cloud droplets and the chaff. However, comparing Doppler spectra obtained from chaff alone and cloud droplets alone illustrates the differences in the signals from

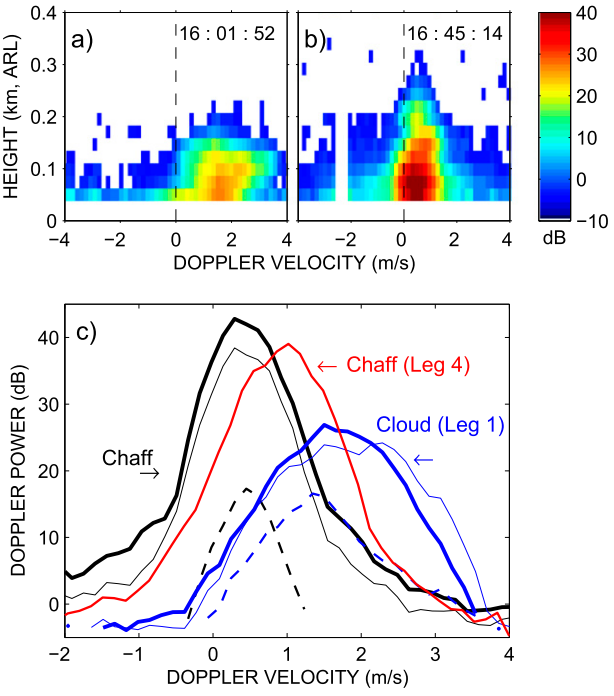

FIG. 7. Vertical profiles of Doppler power obtained (a) during leg 1 from cloud droplets and (b) from chaff returns on 2 Apr in the clear-air boundary layer. (c) Doppler power at a given height. Black is used for chaff returns in the clear-air boundary layer, red is for leg 4 (the corresponding Doppler power is shown in Fig. 8), and blue is for cloud returns during leg 1 at the heights of maximum strength (thick lines), second maximum strength (thin lines), and at the edge of cloud/chaff (dashed lines).

each, which can then be used to identify the dominant reflectors. The differences between hydrometeor radar returns and chaff returns are illustrated in Fig. 7 by using the differences in Doppler spectra between chaff and cloud droplets.

Doppler spectra obtained during leg 1 at 1601:51 UTC, when the returned signals were exclusively from the cloud droplets, are used as an example of hydrometeor radar returns. The signatures of these returns are compared with those sampled on 2 April when chaff was released in clear-sky areas. Doppler spectra obtained during leg 4 at 1609:14 UTC—a case of a dissipating cloud with no observed liquid water at the time of chaff observation—are also used as an example for the chaff returns. In Fig. 7, some differences in the Doppler spectra are observed. First, the strength of the signal obtained from the chaff alone (Fig. 7b and black lines in Fig. 7c) is significantly stronger than that from cloud droplets alone (Fig. 7a and blue lines in Fig. 7c). Second, returns from cloud droplets show broader Doppler power spectra compared with those from the chaff. For example, if we compare the Doppler powers obtained at the edges of the cloud (the weakest signal in Fig. 7; shown by a dashed line), the Doppler velocity of the chaff returns varies from -0.1 to $1.0\,\mathrm{m\,s^{-1}}$ at the 5-dB level. But the Doppler velocity of cloud droplets varies from 0.3 to $2.6\,\mathrm{m\,s^{-1}}$ at the same 5-dB level, indicating an additional broadening of Doppler velocity due to the size variability in the cloud droplets.

In the absence of hydrometeors, spectrum width (i.e., the variation of Doppler velocities) is a minimum as shear, turbulence, and variations in droplet fall speeds all contribute to the broadening of the spectrum width (e.g., Kollias et al. 2001). In a related context, Chandra et al. (2010) showed narrow spectrum widths of insects compared with those of fair-weather continental cumuli. In their study, a vertically pointing Doppler cloud radar was used to monitor the properties of the boundary layer turbulence, and insects were treated as passive scatterers that follow the mean vertical air motion in the same way that the chaff does in our study. As discussed above, the aircraft motion contributes to the broadening of the spectrum width, too. Here, for a beamwidth of 0.7° and an aircraft speed of $\sim 60\,\mathrm{m\,s^{-1}}$, a broadening of the spectrum width of $\sim 0.7\,\mathrm{m\,s^{-1}}$ is expected. However, this artificial broadening applies equally to all parts of the returns; thus, this broadening will be the same for both the chaff and the cloud returns. Therefore, the broadening of the spectrum width due to the aircraft motion cannot contribute to the differences in Doppler spectra between the cloud droplets and chaff discussed here. Third, the Doppler spectrum from cloud droplets shows a bell-shaped pattern and it is slightly skewed toward positive velocities, particularly at the edge of the cloud tops (long tails toward positive V_r). The shape of the Doppler power obtained exclusively from chaff (black) is close to a Gaussian distribution, which is consistent with a broadening due to the turbulence within the sampling volume of the radar beam.

The chaff returns obtained during leg 4 for a case when the cloud is almost dissipated show a similar Gaussian shape of Doppler power with a strength similar to that of the chaff alone. The returns from leg 4 show slightly broader Doppler velocity distributions compared with those from the chaff alone, but with narrower distributions compared with those from the cloud droplets alone. In short, chaff returns obtained from almost dissipated clouds (i.e., leg 4) show the strength of returns similar to the chaff-alone returns, but with the spectrum widths falling between the chaff-alone and cloud-droplets-alone returns. Using the differences in Doppler spectra between chaff and cloud droplets, for the case studied here, *we used the combination of both high reflectivities and narrow spectrum widths as*

indicating the dominance of chaff in the radar signal. Both conditions should be satisfied; and it is not true for either of them alone. Further, to illustrate flows in and around the small cumulus clouds, we utilized both cloud droplets and chaff returns in the next section. Chaff alone serves as a tracer outside the cloud where no cloud droplets exist, but both chaff and cloud droplets serve as tracers inside the cloud to give an idea of the in-cloud flow patterns.

2) CHAFF RETURNS

The radar reflectivity of the chaff, observed during legs 3 and 4, which were flown at 300 and 450 m below the level of chaff releases, is shown in Fig. 6. Time–height cross sections of reflectivity during leg 3 (Fig. 6b) show two areas of strong reflectivity (e.g., $Z > -20$ dBZ) caused by radar chaff: 1) along the outside of the cloud edges with a vertically elongated pattern near identifier A and 2) at the borders of the cloud (based on LWC) with a circular shape near identifier B. In the Doppler velocity field (Fig. 6c), downward motion of $\sim$1 m s^{-1} is associated with a vertically elongated area of chaff signals (near A), indicating that chaff is descending to lower heights along the downshear side of the cloud edge. The downward-moving feature along the cloud edge in Fig. 6c (between 1.2 and 1.4 km) is consistent with the downdraft area observed from the in situ aircraft observations during legs 1 and 2 (Figs. 5a,e), and is in an area where no liquid water is observed.

Relative to the regions containing cloud droplets (e.g., sw $\sim >$ 1 m s^{-1} in Fig. 6d near identifier E), the spectrum widths are relatively small in the areas where the chaff signals are observed (e.g., sw $\sim >$ 0.5 m s^{-1} in Fig. 6d near identifier A). In contrast, large spectral widths are observed along the cloud edges and beneath the detached cloud turrets, suggesting that variations in droplet fall speeds, active turbulent mixing, or horizontal shear of the vertical velocity in these region lead to a broadening of the Doppler spectrum.

The circular-shaped area of strong chaff reflectivity in Fig. 6b (centers near identifiers B and C) was observed outside the cloud penetrated by the aircraft. In Fig. 6b, cloud boundaries (shown in Fig. 9) extend from near the identifier A at 1606:18 UTC at the lowest radar level. These cloud boundaries inferred from the radar returns (identifier A at 1606:18 UTC) differ from those estimated from aircraft observations (i.e., cloud boundaries estimated from LWC are near identifier C at 1606:12 UTC in Fig. 6b), since the lowest height at which the radar acquires data is about 50 m above the height of the aircraft. In addition, the cloud studied here is tilted westward with height and consists of multiple small thermals. The circular-shaped chaff returns (Fig. 6b) are found in updrafts in Fig. 6c; updrafts of $\sim$2 m s^{-1} are observed near identifier C; otherwise, $V_r \sim 0$ m s^{-1} is observed overall. In Fig. 6b, a relatively strong radar return ($Z \sim -20$ dBZ) is seen separately from the main chaff signal, between identifiers D and E (closer to D), which corresponds to the edge of the updraft area centered on identifier E. This feature implies that the area of strong chaff reflectivity in Fig. 6b connects to the rising branch of echoes along the upshear side of the cloud with reflectivities of ~ -28 dBZ (yellowish colors in Fig. 6b) and updrafts stronger than 1 m s^{-1} in Fig. 6c. As time proceeds, the cloud is filled with chaff as shown in the reflectivity field (Fig. 6f). The right half of the cloud shows predominately updrafts, particularly during leg 3 (near identifier E in Fig. 6c), and the left half of the cloud shows downward motions, particularly along the downshear side of the cloud edges (e.g., B in Fig. 6c, and D in Fig. 6g). Overall, spectrum widths within the chaff-filled cloud (Fig. 6h) are small (e.g., sw $<$ 1 m s^{-1}). A detailed analysis of how chaff entrains into the main cloud and comparisons of the radar signals from chaff and cloud droplets is shown in Fig. 8 for legs 2–4.

During leg 2 (Fig. 8, first row), updrafts of about 0–3 m s^{-1} are detected in most parts of the cloud area, and downdrafts are observed at the edge of the cloud. The clouds and Doppler spectra observed during leg 2 are unaffected by chaff and, thus, the returns are exclusively from cloud droplets.

To compare the Doppler power obtained from the chaff and cloud droplets during leg 3, their Doppler power spectra are shown in the second row of Fig. 8. The radar returns from chaff (A in the second row), which are represented by a vertically elongated pattern in Fig. 6b, show predominant downward motion. In contrast, updrafts dominate throughout the cloud in E at 1606:15 UTC. Further, the differences between the strengths of the returns are as large as previously shown in Fig. 7.

Snapshots of how chaff entrains into the main cloud are shown in the third row for leg 3 through B to C3. At point B, downward and upward motions ($-2 < V_r < 1$ m s^{-1}) are found in areas with strong returns. However, from C1 to C3, vertical velocities shift to upward motion, especially near the flight level (the lowest radar heights). At point D2, the top part of the chaff signals (slightly below 0.2 km) continues to move upward (and connects to the rising branch of cloudy air seen in Fig. 6b). Through C2 to C3, the top part of the main cloud [0.2–0.3 km above radar level (ARL)] tends to tilt to the left with downward motions emerging from the cloud tops. This feature is more evident in E (second row of Fig. 8).

Doppler spectra, obtained from leg 4, are shown in the fourth row. Updrafts dominate the lower levels but,

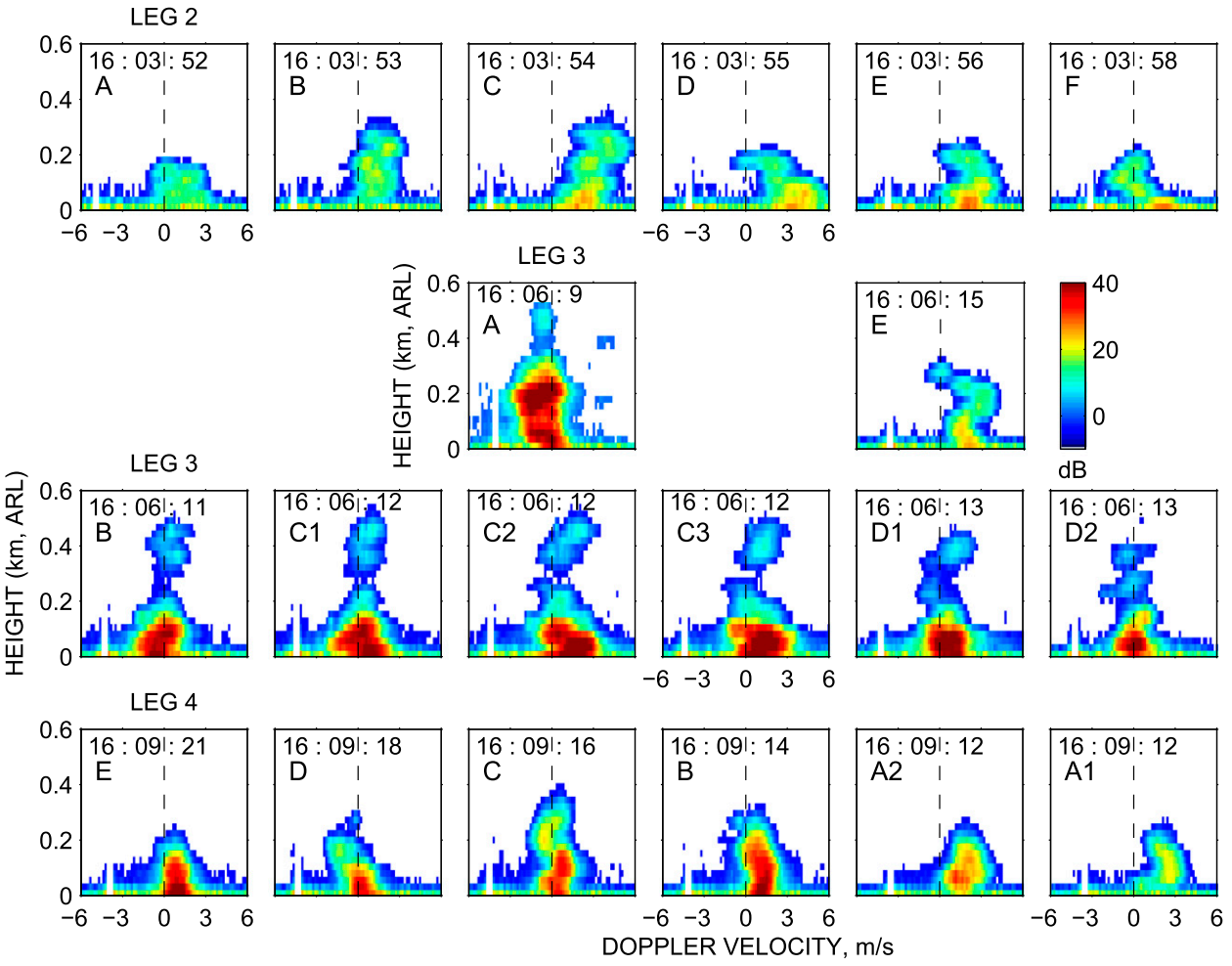

FIG. 8. As in Figs. 7a,b, but for data corresponding to legs 2–4 ARL. Zero velocity is shown by the vertical dashed line. Letter identifiers (A–E) correspond to locations and times for each leg shown in Figs. 5f, 6b, and 6f, with letter–number identifiers (e.g., C1, C2, C3) relating to subsets of the time period associated with that letter.

as the aircraft transits the cloud (from A to D; right to left) downdrafts are observed near the cloud top from the latter half of the cloud (C and D). Signals in A1 are mainly associated with cloud droplets where liquid water is observed at the flight level (see Fig. 6f) and the strength of the reflectivity is relatively weak compared with signals from the chaff (e.g., B in leg 4). Signals from A2 are possibly the result of a combination of clouds and chaff returns because the strength of the radar returns in A2 is stronger than those obtained from cloud droplets (e.g., A1 from leg 4), but liquid water is observed in A (Fig. 6h). In addition, the Doppler velocity spans a larger range compared with that observed in A1. Although we cannot separate the returns from the cloud and chaff without radar polarimetric capabilities, the separation incapability does not alter the results that we address here because we use both chaff and cloud returns to infer the circulations in and around the cloud. The strong returns from B and E (at least at the lowest level) are mainly associated with chaff since no cloud water is observed at the flight level (Fig. 6f). From B to D (above 0.1 km ARL), the upper portion of the cloud tilts to the left with height (downshear) and is the origin of downward motions, implying circulations near the downshear flank of the cloud base that originated from the cloud top.

The chaff tracers facilitate the identification of in-cloud flows as well as flows around the cloud. The cloud circulations inferred from the radar observations are summarized in Fig. 9 as a schematic. In this schematic the environmental air descends to near the lower observational level along the downshear side of the cloud flank (denoted as 1–2). A blob of chaff (circular shape) is engulfed into the cloud (denoted as 2–3) with the aid of updrafts (refer to V_r around 1606:12 UTC in Fig. 6c). Once entrained into the cloud, the air parcels move to

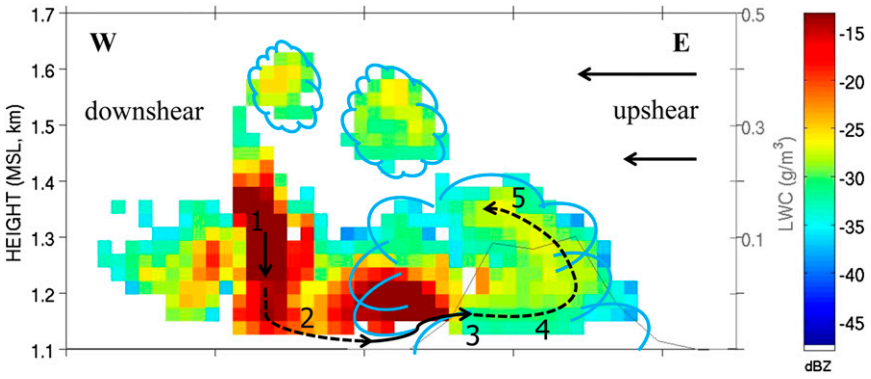

FIG. 9. Schematic of the entrainment processes and in-cloud flow pattern for a shallow marine cumulus cloud; overlaid is the radar reflectivity field observed during leg 3. Cloud boundaries are shown as blue solid lines, while chaff movements and in-cloud flow patterns are denoted as black solid and dashed lines. Background winds are denoted as arrows to show the upshear/downshear direction. The letters E and W in the top corners indicate east and west, respectively. The 1-Hz-resolution LWCs are added as thin black solid lines.

the upshear cloud flank (denoted as 4). On the upshear cloud flank, air parcels move upward to the cloud top along the cloud edges through updrafts (denoted as 5). Finally, the air follows the downward motions along the downshear side of the cloud edges. The in-cloud flow follows the inverted letter P pattern shown in Fig. 4 of Kitchen and Caughey (1981) and also that shown by Zhao and Austin (2005). Detrained cloud elements are also seen above the main cloud. Among the limitations of this experiment, however, is that the chaff was released near the cloud top but not far above the cloud top. As a result, the cloud-top entrainment described by Blyth et al. (1988, Fig. 14) may not be fully illustrated by our results, although the circulation implied may be closer to those described by Jonas (1990).

d. *Entrainment levels*

To determine if the circulation pattern inferred from the chaff is dynamically possible, we examine the time series of the potential temperature at the different height levels. The potential temperatures during leg 1 (downwind), leg 2 (crosswind), and leg 3 (upwind) are shown in Fig. 10. Environmental potential temperatures, obtained from the nearest soundings (in time and space) at the heights of leg 3, are overlaid as horizontal dashed lines.

In Fig. 10a, potential temperature (cold) peaks at around 301.1 K on the exit side of the cloud during leg 1 (near 1601:53–54 UTC). But this temperature drop was exaggerated by about 0.4 K since the temperature sensor experienced artificial cooling when it exited the cloud, as discussed in Wang and Geerts (2009). During legs 2 and 3, potential temperatures measured in the cloud shell (just outside the cloudy air) are around 301.5 K on the entrance side (301.5–301.6 K for leg 2 and 301.3–301.5 K for leg 3). Figure 10 shows that the potential temperatures from legs 1–3 are approximately equal to those of the environmental soundings (300.9–301.3 K, shown by the dashed lines) on the downshear side of the cloud edges, where the chaff was entrained into the cloud on leg 3 (e.g., Fig. 6b), implying that the shell air (which is chaff) descends to the level of temperature equilibrium (i.e., height of leg 3). During leg 3, the air in the cloud shell is warmer than that of the environment, which is consistent with the adiabatic descent and warming of dry air in the shell. The arguments about buoyancy would be slightly modified if virtual effects were considered. However, the slow response of the humidity sensor prevents the use of virtual temperature on the downdraft areas near the cloud boundaries; we also assumed that the dry air in the cloud shell area is never cloudy.

4. Summary and conclusions

In this study, the feasibility of using chaff with an airborne cloud radar to study entrainment processes and circulations in and around a small cumulus cloud is demonstrated. A shallow trade-wind cumulus cloud that was observed about 100 km east of Barbados on 29 March 2010 is investigated to demonstrate this technique. The radar chaff elements used for this experiment are fibers that are cut to a length of about ½ of the radar wavelength to maximize radar returns by serving as dipole antennas.

The chaff was released near the cloud tops and along the edges of the cloud during level flight legs (legs 1 and 2). The aircraft then descended and made penetrations of the chaffed cloud at lower levels to observe the chaff above

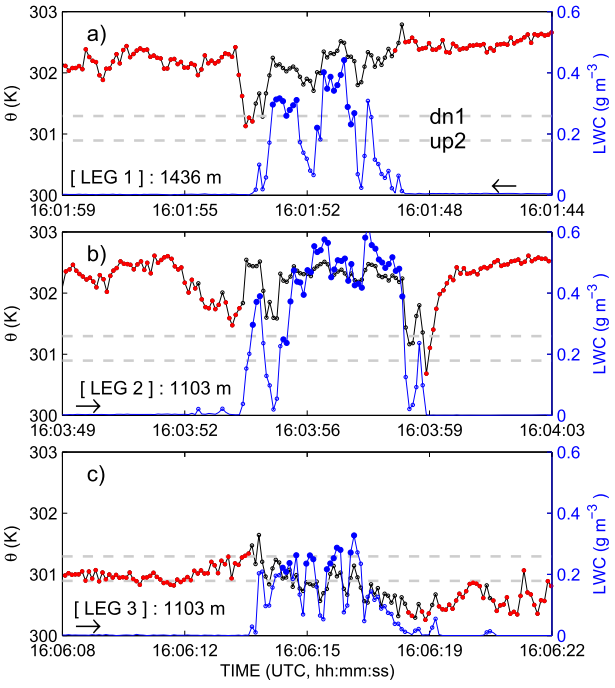

FIG. 10. Time series of potential temperature (black and red) and LWC (blue) for legs (a) 1, (b) 2, and (c) 3, with environmental potential temperatures (horizontal dashed lines) at the heights of leg 3, obtained from the two closest soundings in time and space during the flights. Note that a reversed time axis is used during leg 1. Blue-filled dots indicate samples representing saturated, cloudy air defined as having a Gerber-probe-determined LWC $>$ 0.2 g m^{-3} and cloud droplet number concentrations obtained from CAS $>$ 50 cm^{-3}. Potential temperatures outside the cloud (LWC $<$ 0.01 g m^{-3}) are shown by red-filled dots. Flight direction is shown by horizontal arrows.

with an airborne cloud radar. Since the terminal velocity of the chaff fibers is about 2 cm s^{-1}, the chaff effectively tracks with air motions; thus, radar returns from the chaff illustrate the flows in and around the cloud.

The environmental air above the cloud top, tagged with chaff tracers, appears to descend dry adiabatically to the level of temperature equilibrium (i.e., leg 3) along the downshear cloud flank and, subsequently, is entrained into the growing cloud. Then, the radar chaff observations suggest that the entrained air circulates along the in-cloud edges with an inverted letter P shape, showing a complete picture of the in-cloud flow pattern. This pattern is consistent with the flow patterns in Kitchen and Caughey (1981) and Zhao and Austin (2005) in a sheared environment. In addition, the cloud circulations implied in this study agree with the findings of Jonas (1990) and Stith (1992). These results differ with those from Blyth et al. (1988), where entrainment occurs near the cloud top and the mixed parcels descend around the edge of thermal core inside the cloud.

In this study, we used radar returns from both cloud droplets and chaff to illustrate flows in and around the small cumulus clouds. Chaff alone played a role as a tracer outside the cloud where no cloud droplets exist, while both chaff and cloud droplets played roles as tracers inside the cloud to give an idea of in-cloud flow patterns. Observations in noncloudy air in this study, using chaff tracers, showed how the methods suggested by Moninger and Kropfli can be applied to the problem of entrainment in cumulus clouds. However, the one-dimensional vertically pointing cloud radar used here is limited in providing the time–space distribution of both chaff and cloud. A scanning cloud radar would allow a full view of the 3D temporal evolution of the cloud and the chaff. Further, chaff reflectivity becomes easily indistinguishable from hydrometeor reflectivity (e.g., raindrops) if the chaff enters the vigorous cloud whose reflectivity is as strong as those from the chaff returns (e.g., thunderstorm). Therefore, radar with differential polarization capabilities would allow for an effective separation of the chaff from the hydrometeor returns, as discussed by Moninger and Kropfli (1987) and Zrnić and Ryzhkov (2004).

Acknowledgments. We are grateful for the dedicated efforts of all the individuals who made the observations from the CIRPAS Twin Otter during BACEX. A special thanks is given to the onboard scientist, Graham Feingold, who provided key scientific input on the observing strategies employed on this particular day and the aircraft chief scientist, Haflidi Jonsson, for his help with the aircraft data. We thank Alan Blyth and two anonymous reviewers for their constructive and comprehensive comments on the manuscript. It has been improved considerably by their comments and suggestions. We also thank Robert Seigel for helpful discussion and comments. This study was funded by ONR Grant N000140810465.

REFERENCES

Baker, M., R. G. Corbin, and J. Latham, 1980: The influence of entrainment on the evolution of cloud droplet spectra. 1. A model of inhomogeneous mixing. *Quart. J. Roy. Meteor. Soc.,* **106,** 581–598, doi:10.1002/qj.49710644914.

Bladé, I., and D. L. Hartmann, 1993: Tropical intraseasonal oscillations in a simple nonlinear model. *J. Atmos. Sci.,* **50,** 2922–2939, doi:10.1175/1520-0469(1993)050<2922:TIOIAS>2.0.CO;2.

Blyth, A. M., 1993: Entrainment in cumulus clouds. *J. Appl. Meteor.,* **32,** 626–641, doi:10.1175/1520-0450(1993)032<0626:EICC>2.0.CO;2.

——, W. A. Cooper, and J. B. Jensen, 1988: A study of the source of entrained air in Montana cumuli. *J. Atmos. Sci.,* **45,** 3944–3964, doi:10.1175/1520-0469(1988)045<3944:ASOTSO>2.0.CO;2.

Carpenter, R. L., K. K. Droegemeier, and A. M. Blyth, 1998: Entrainment and detrainment in numerically simulated

cumulus congestus clouds. Part III: Parcel analysis. *J. Atmos. Sci.,* **55,** 3440–3455, doi:10.1175/1520-0469(1998)055<3440:EADINS>2.0.CO;2.

Chandra, A. S., P. Kollias, S. E. Giangrande, and S. A. Klein, 2010: Long-term observations of the convective boundary layer using insect radar returns at the SGP ARM Climate Research Facility. *J. Climate,* **23,** 5699–5714, doi:10.1175/2010JCLI3395.1.

Cooper, W. A., S. G. Lasher-Trapp, and A. M. Blyth, 2013: The Influence of entrainment and mixing on the initial formation of rain in a warm cumulus cloud. *J. Atmos. Sci.,* **70,** 1727–1743, doi:10.1175/JAS-D-12-0128.1.

Damiani, R., G. Vali, and S. Haimov, 2006: The structure of thermals in cumulus from airborne dual-Doppler radar observations. *J. Atmos. Sci.,* **63,** 1432–1450, doi:10.1175/JAS3701.1.

Dehghan, A., and W. K. Hocking, 2011: Instrumental errors in spectral-width turbulence measurements by radars. *J. Atmos. Sol. Terr. Phys.,* **73,** 1052–1068, doi:10.1016/j.jastp.2010.11.011.

Eastin, M. D., P. G. Black, and W. M. Gray, 2002: Flight-level thermodynamic instrument wetting errors in hurricanes. Part I: Observations. *Mon. Wea. Rev.,* **130,** 825–841, doi:10.1175/1520-0493(2002)130<0825:FLTIWE>2.0.CO;2.

Frisch, A. S., C. W. Fairall, and J. B. Snider, 1995: Measurement of stratus cloud and drizzle parameters in ASTEX with a K_α-band Doppler radar and a microwave radiometer. *J. Atmos. Sci.,* **52,** 2788–2799, doi:10.1175/1520-0469(1995)052<2788:MOSCAD>2.0.CO;2.

Gerber, H., B. G. Arends, and A. S. Ackerman, 1994: New microphysics sensor for aircraft use. *Atmos. Res.,* **31,** 235–252, doi:10.1016/0169-8095(94)90001-9.

——, G. M. Frick, J. B. Jensen, and J. G. Hudson, 2008: Entrainment, mixing, and microphysics in trade-wind cumulus. *J. Meteor. Soc. Japan,* **86A,** 87–106, doi:10.2151/jmsj.86A.87.

Heus, T., and H. J. J. Jonker, 2008: Subsiding shells around shallow cumulus clouds. *J. Atmos. Sci.,* **65,** 1003–1018, doi:10.1175/2007JAS2322.1.

——, G. van Dijk, H. J. J. Jonker, and H. E. A. Van den Akker, 2008: Mixing in shallow cumulus clouds studied by Lagrangian particle tracking. *J. Atmos. Sci.,* **65,** 2581–2597, doi:10.1175/2008JAS2572.1.

Jensen, J. B., and A. M. Blyth, 1988: Comment on ''Mixing mechanisms in cumulus congestus clouds. Part I: Observations.'' *J. Atmos. Sci.,* **45,** 2460–2463, doi:10.1175/1520-0469(1988)045<2460:COMICC>2.0.CO;2.

Johari, H., 1992: Mixing in thermals with and without buoyancy reversal. *J. Atmos. Sci.,* **49,** 1412–1426, doi:10.1175/1520-0469(1992)049<1412:MITWAW>2.0.CO;2.

Jonas, P. R., 1990: Observations of cumulus cloud entrainment. *Atmos. Res.,* **25,** 105–127, doi:10.1016/0169-8095(90)90008-Z.

Jung, E., 2012: Aerosol-cloud-precipitation interactions in the trade wind boundary layer. Ph.D. dissertation, University of Miami, 184 pp. [Available online at http://scholarlyrepository.miami.edu/oa_dissertations/900.]

——, B. A. Albrecht, J. M. Prospero, H. H. Jonsson, and S. M. Kreidenweis, 2013: Vertical structure of aerosols, temperature and moisture associated with an intense African dust event observed over the eastern Caribbean. *J. Geophys. Res. Atmos.,* **118,** 4623–4643, doi:10.1002/jgrd.50352.

Kitchen, M., and S. J. Caughey, 1981: Tethered-balloon observations of the structure of small cumulus clouds. *Quart. J. Roy. Meteor. Soc.,* **107,** 853–874, doi:10.1002/qj.49710745407.

Kollias, P., B. A. Albrecht, R. Lhermitte, and A. Savtchenko, 2001: Radar observations of updrafts, downdrafts, and turbulence in fair weather cumuli. *J. Atmos. Sci.,* **58,** 1750–1766, doi:10.1175/1520-0469(2001)058<1750:ROOUDA>2.0.CO;2.

Lasher-Trapp, S., W. A. Cooper, and A. M. Blyth, 2005: Broadening of droplet size distributions from entrainment and mixing in a cumulus cloud. *Quart. J. Roy. Meteor. Soc.,* **131,** 195–220, doi:10.1256/qj.03.199.

Lehmann, K., H. Siebert, and R. A. Shaw, 2009: Homogeneous and inhomogeneous mixing in cumulus clouds: Dependence on local turbulence structure. *J. Atmos. Sci.,* **66,** 3641–3659, doi:10.1175/2009JAS3012.1.

Lu, C., Y. Liu, and S. Niu, 2011: Examination of turbulent entrainment mixing mechanisms using a combined approach. *J. Geophys. Res.,* **116,** D20207, doi:10.1029/2011JD015944.

Moninger, W. R., and R. A. Kropfli, 1987: A technique to measure entrainment in cloud by dual-polarization radar and chaff. *J. Atmos. Oceanic Technol.,* **4,** 75–83, doi:10.1175/1520-0426(1987)004<0075:ATTMEI>2.0.CO;2.

Nastrom, G. D., 1997: Doppler radar spectral width broadening due to beamwidth and wind shear. *Ann. Geophys.,* **15,** 786–796, doi:10.1007/s00585-997-0786-7.

Paluch, I. R., 1979: The entrainment mechanism in Colorado cumuli. *J. Atmos. Sci.,* **36,** 2467–2478, doi:10.1175/1520-0469(1979)036<2467:TEMICC>2.0.CO;2.

Rauber, R. M., and Coauthors, 2007: Rain in shallow cumulus over the ocean: The RICO campaign. *Bull. Amer. Meteor. Soc.,* **88,** 1912–1928, doi:10.1175/BAMS-88-12-1912.

Romps, D. M., and Z. Kuang, 2010: Nature versus nurture in shallow convection. *J. Atmos. Sci.,* **67,** 1655–1666, doi:10.1175/2009JAS3307.1.

Stith, J. L., 1992: Observations of cloud-top entrainment in cumuli. *J. Atmos. Sci.,* **49,** 1334–1347, doi:10.1175/1520-0469(1992)049<1334:OOCTEI>2.0.CO;2.

Wang, Y., and B. Geerts, 2009: Estimating the evaporative cooling bias of an airborne reverse flow thermometer. *J. Atmos. Oceanic Technol.,* **26,** 3–21, doi:10.1175/2008JTECHA1127.1.

——, ——, and J. French, 2009: Dynamics of the cumulus cloud margin: An observational study. *J. Atmos. Sci.,* **66,** 3660–3677, doi:10.1175/2009JAS3129.1.

Zhao, M., and P. H. Austin, 2005: Life cycle of numerically simulated shallow cumulus clouds. Part II: Mixing dynamics. *J. Atmos. Sci.,* **62,** 1291–1310, doi:10.1175/JAS3415.1.

Zrnić, D. S., and A. V. Ryzhkov, 2004: Polarimetric properties of chaff. *J. Atmos. Oceanic Technol.,* **21,** 1017–1024, doi:10.1175/1520-0426(2004)021<1017:PPOC>2.0.CO;2.